Saturn's Dusty Ionosphere

M. W. Morooka, J.- E. Wahlund, Lina Hadid, A. I. Eriksson, N. J. T. Edberg, E. Vigren, D. J. Andrews, A. M. Persoon, W. S. Kurth, D. A Gurnett, et al.

AGU100 ADVANCING EARTH AND SPACE SCIENCE

JGR Space Physics

RESEARCH ARTICLE
10.1029/2018JA026154

Key Points:
- In situ measurements of Saturn's ionospheric plasma densities down to 1,500 km and the ring above the ionosphere is presented
- Charge imbalance in the ions and electrons, evidence of the negatively charged heavy particles, has been observed below 2,500 km
- Observations suggest that Saturn's ionosphere consists of a significant amount of negatively and positively charged heavy ions

Correspondence to:
M. W. Morooka,
morooka@irfu.se

Citation:
Morooka, M. W., Wahlund, J.-E., Hadid, L. Z., Eriksson, A. I., Edberg, N. J. T., Vigren, E., et al. (2019). Saturn's dusty ionosphere. *Journal of Geophysical Research: Space Physics*, *124*, 1679–1697. https://doi.org/10.1029/2018JA026154

Received 2 OCT 2018
Accepted 21 FEB 2019
Accepted article online 7 MAR 2019
Published online 22 MAR 2019

Saturn's Dusty Ionosphere

M. W. Morooka[1], J.-E. Wahlund[1], L. Z. Hadid[1], A. I. Eriksson[1], N. J. T. Edberg[1], E. Vigren[1], D. J. Andrews[1], A. M. Persoon[2], W. S. Kurth[2], D. A. Gurnett[2], W. M. Farrell[3], J. H. Waite[4], R. S. Perryman[4], and M. Perry[5]

[1]Swedish Institute of Space Physics, Uppsala, Sweden, [2]Department of Physics and Astronomy, University of Iowa, Iowa City, IA, USA, [3]NASA Goddard Space Flight Center, Greenbelt, MD, USA, [4]Southwest Research Institute, San Antonio, TX, USA, [5]The Johns Hopkins University Applied Physics Laboratory, Laurel, MD, USA

Abstract Measurements of electrons and ions in Saturn's ionosphere down to 1,500-km altitudes as well as the ring crossing region above the ionosphere obtained by the Langmuir probe onboard the Cassini spacecraft are presented. Five nearly identical deep ionosphere flybys during the Grand Finale orbits and the Final plunge orbit revealed a rapid increase in the plasma densities and discrepancies between the electrons and ions densities (N_e and N_i) near the closest approach. The small N_e/N_i ratio indicates the presence of a dusty plasma, a plasma which charge carrier is dominated by negatively charged heavy particles. Comparison of the Langmuir probe obtained density with the light ion density obtained by the Ion and Neutral Mass Spectrometer confirmed the presence of heavy ions. An unexpected positive floating potential of the probe was also observed when $N_e/N_i \ll 1$. This suggests that Saturn's ionosphere near the density peak is in a dusty plasma state consisting of negatively and positively charged heavy cluster ions. The electron temperature (T_e) characteristics in the ionosphere are also investigated and unexpectedly high electron temperature value, up to 5000 K, has been observed below 2,500-km altitude in a region where electron-neutral collisions should be prominent. A well-defined relationship between T_e and N_e/N_i ratio was found, implying that the electron heating at low altitudes is related to the dusty plasma state of the ionosphere.

Plain Language Summary Cassini Langmuir probe measurements revealed ion densities in excess of the electron densities, indicative of a dusty plasma, in Saturn's ionosphere below 2,500-km altitude. Comparison of the Langmuir probe measurements with those of the Ion and Neutral Mass Spectrometer, sensitive to only lighter ions during this period, showed that heavy ions dominate in this region. Positive spacecraft potentials were also found, suggesting that Saturn's ionosphere contains dusty plasma of negatively and positively charged heavy ions.

1. Introduction

Before Cassini's Grand Finale orbits, the density of Saturn's ionospheric plasma had been investigated only with remote sensing that provided altitude profiles of the electron densities, with a peak density of about 10^3 cm^{-3} at altitudes of ~1,000 km (Kliore et al., 2009; Nagy et al., 2006). (The common definition of zero altitude is Saturn's 1-bar surface, 60,268 km from the center of the planet at the equator.) On the other hand, these observed values were 2 orders of magnitudes smaller than the value expected from ionospheric models (e.g., McElroy, 1973). The "ring rain" hypothesis, the idea that the effect of water molecules from the icy rings could further reduce the long-lived H^+ (Connerney & Waite, 1984; Moore et al., 2015; O'Donoghue et al., 2013), could explain the observed electron deficiency.

In April 2017, the Cassini spacecraft began the Grand Finale orbits and provided the first in situ measurements of the plasma between the ionosphere and the D ring of Saturn. The data from its first flyby showed a predominance of H^+ ions at altitudes as low as 3,000 km and did not show any evidence of the ring rain effect. Data from other orbits that crossed the ring plane at altitudes between 2,500 and 4,500 km showed heavy ions around the D ring (Wahlund et al., 2017). The effect of the ring material on the atmosphere remained an open question.

The 22 flybys of the Grand Finale orbits were used to construct the altitude profiles of the electron density near the equator. The obtained electron density has different scale heights depending on the altitude and revealed a three-layered structure. The electron densities were stable below the altitude of 2,500 km, a region interpreted as the chemistry dominant region where photochemical equilibrium is achieved. Above

2,500 km the density values had a large variation possibly related to the interaction between the ionosphere and the D ring. The region above 4,500 km is interpreted as the transport dominant region with a significant north/south asymmetry due to the ring shadow effects (Hadid et al., 2018; Persoon et al., 2018). Although the obtained electron density structure was similar to the classic picture (Schunk & Nagy, 2009), a charge imbalance between the electrons and the light mass ions has been found at low altitudes (Waite et al., 2018), indicating a complex chemistry process with heavy ions (Cravens et al., 2018; Moore et al., 2018).

Contrary to the significant amount of electron density measurements, there had been no direct observations of the plasma temperatures in the ionosphere of the giant planets. The plasma temperature of Saturn's ionosphere has been instead inferred based on the electron density profiles that provides a scale height. While this method gives a rough estimate of the temperature over a large altitude scale in the transport controlled topside ionosphere, it cannot explain the observed small scale density variations (Kliore et al., 2009) nor give the plasma temperature within the chemistry controlled ionosphere.

A couple of modeling efforts have been reported regarding Saturn's electron temperature profile. Moore et al. (2008) used the Saturn Thermosphere Ionosphere Model to calculate the temperature of ions and electrons self-consistently, mainly at altitudes below 3,000 km. They investigated the effect of different neutral temperatures and different extreme ultraviolet (EUV) intensities that can cause the local time dependencies in ionization. Their results predicted a maximum electron temperature of around 500 K in the altitude range 1,500–3,000 km. Sakai and Watanabe (2016) used a parameterized heating/cooling rate to model the altitude profile of the electron temperature. Their model considered the heat flow from the magnetosphere in addition to the chemistry of the atmosphere and therefore predicted the temperatures of up to 10,000 K at high altitudes, above 6,000 km.

During the last five orbits of the Grand Finale and the final plunge into the atmosphere, the perikrone altitudes ranged from below 3,000 km down to 1,400 km. The ionospheric electron density observation during the Grand Finale near the equator detected an ionospheric electron density peak just above 1,500-km altitudes (Hadid et al., 2018; Persoon et al., 2018). This altitude is close to the electron density peak previously observed using the radio occultation technique (Kliore et al., 2009).

The Radio and Plasma Wave Science (RPWS) instrument onboard Cassini (Gurnett et al., 2004) includes the Langmuir probe (LP) that provides in situ measurements of the densities of the electrons and the ions and the electron temperature. In this paper, we report on the characteristics of the electron and ion densities as well as the electron temperature obtained by the LP during the Grand Finale orbits. The RPWS measurements of the ion and electron densities were also compared with the density of the light ions (mass less than 4 amu) measured by the Ion and Neutral Mass Spectrometer (INMS; Waite et al., 2018). The data set in this study shows new results that indicate the dusty plasma characteristics of Saturn's ionosphere. The LP observed that the total ion density exceeded the electron density that indicates the presence of the unseen negatively charged particles, which in addition to the electrons, are required to maintain charge balance. The six sets of electron and ion density profiles below 4,000-km altitudes show a consistent picture of the electron to ion density ratio (N_e/N_i) decreasing as the spacecraft approaches the planet. A positive probe floating potential has been found as N_e/N_i becomes smaller, which suggests that the positively and negatively charged heavy ions are the dominant charge carriers in Saturn's ionosphere. We present also the electron temperature characteristics and compare them with the models by Moore et al. (2008) and Sakai and Watanabe (2016).

In the following section 2, the basic analysis technique and the error estimation of the Cassini/LP data will be first presented. An overview of the RPWS observations during the low-altitude Grand Finale orbits will be presented in section 3, and the validation of the ion density determination will be discussed in sections 4 and 5. The electron and ion density characteristics described in section 2 were consistent for all low-altitude orbits data, which will be presented in section 6. The electron temperature data will be presented in section 7, and section 8 summarizes the results.

2. Langmuir Probe Data Analysis

The Cassini LP is a 5-cm diameter spherical sensor situated 1.5 m from the spacecraft body. When applying a positive or negative bias potential to the LP, it will attract or repel the electrons and ions from the ambient

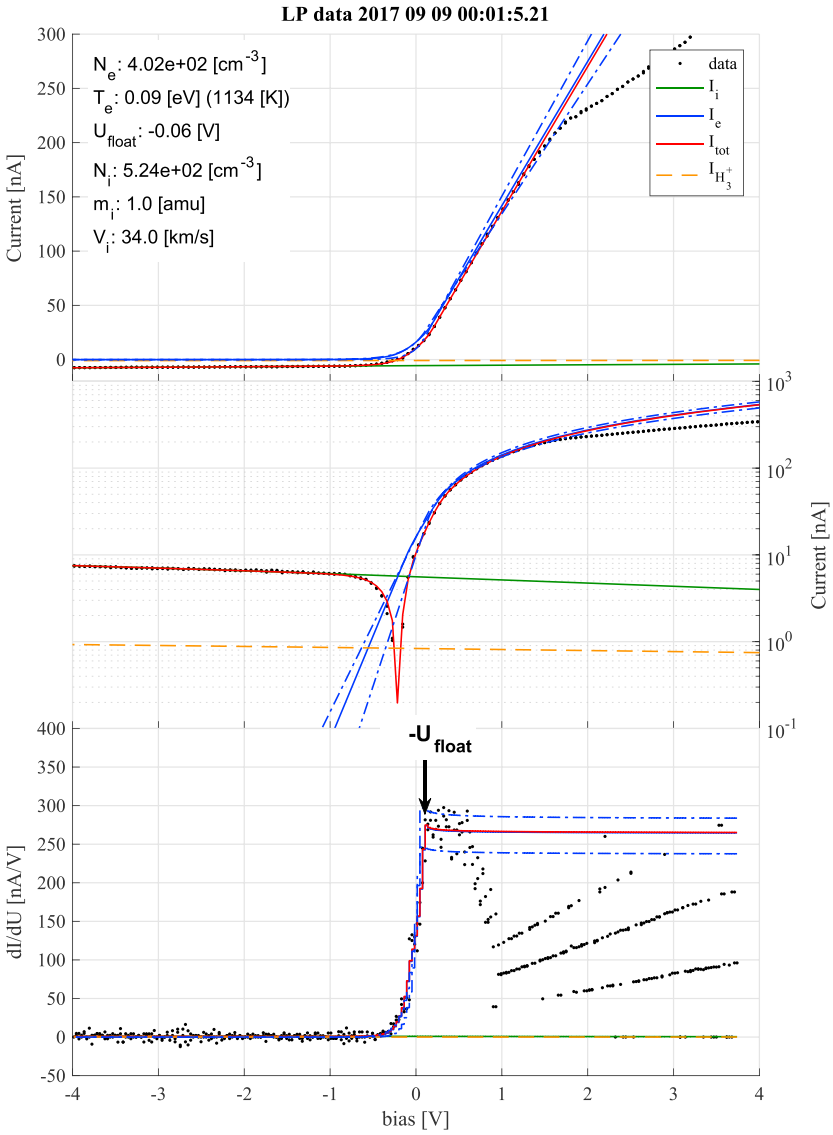

Figure 1. An example of the current–voltage relationship (*I-V* curve) obtained by the Cassini/Radio and Plasma Wave Science Langmuir probe. This sweep was obtained in the topside of Saturn's ionosphere at an altitude of 2,895 km above the 1-bar pressure level. The panels show the same data in linear (top), logarithmic (middle), and first-derivative (bottom) format. The black dots are the observed data. The lines show the fitted ion current (N_i, green), electron current (N_e, blue), and the total current (N_{tot}, red). Blue dashed dot lines are the electron current with the temperature 20% higher/lower than the estimated value. The H_3^+ ion current (orange dashed line) is shown for comparison, obtained using the simultaneous H_3^+ density value obtained by the Ion and Neutral Mass Spectrometer and the spacecraft ram velocity as the ion velocity. The d*I*/d*U* peak, marked with an arrow in the bottom panel, defines U_{float}.

plasma, and the resulting current is measured. During the close planet flybys, the Cassini's LP sampled the current from the ambient plasma every 32 s by setting 256 step bias voltages (U_{bias}) within ±4 V. An example of the current-voltage (*I-V*) characteristics from the LP is shown in Figure 1. This sweep was obtained in Saturn's ionosphere at an altitude of 2,895 km.

By fitting the sampled currents (black dots) to the theoretical curves (green for ions, blue for electrons, and red for the sum of the electrons and ions), the electron and ion parameters were estimated. When the probe bias potential is positive, the probe attracts electrons and repels ions. As a result, the positive voltage biased current represents the electron characteristics (predominantly represents the density, N_e, and also depends on the electron temperature, T_e) and is called the "electron current." A clear exponential response is detected between −0.5 V and $-U_{float}$. This tells us that the electrons are near Maxwellian with well-defined electron

temperature of about 0.09 eV (1134 K). The floating potential, U_{float}, is where the probe electrical potential balances with the ambient plasma. Just above this point the probe potential is greater than the ambient plasma and the sampled current response saturates. The U_{float} point is identified by finding a peak in the derivative of the current (dI/dU, bottom panel). In the case of Figure 1, the dI/dU peak is at 0.16 [V], as indicated by the arrow in the bottom panel of Figure 1, and U_{float} was defined to be −0.16 [V]. We use the orbital motion limited (OML) approximation to fit to the electron current:

$$I_e = eN_eA_{LP}\sqrt{\frac{kT_e}{2\pi m_e}}\exp\left(\frac{-e(U_{\text{float}}+U)}{kT_e}\right). \tag{1}$$

The obtained parameters have inherent errors below 10% for the electron density and the floating potential and errors below 20% for the electron temperature (Gustafsson & Wahlund, 2010). Blue dashed dot lines in Figure 1 are the electron current with the temperature 20% higher/lower than the estimated value. Also, the electron density using the LP sweep technique can at times be up to 30% smaller than the density obtained using the observed plasma wave emissions, such as the upper hybrid lines.

When the probe bias potential is negative, the probe attracts ions and repels electrons, and the current represents the ion characteristics, called the "ion current." The ion current characteristics of an LP onboard a moving vehicle are described in Fahleson (1967):

$$I_i \approx -A_{\text{LP}}n_iq_i\sqrt{\frac{v_i^2}{16}+\frac{k_BT_i}{2\pi m_i}}\left(1-\frac{q_e(U_{\text{float}}+U_{\text{bias}})}{\frac{m_iv_i^2}{2}+k_BT_i}\right), \tag{2}$$

where A_{LP} is the surface area of the LP, and q_i, T_i, n_i, v_i, and m_i are the charge, temperature, density, drift velocity, and mass of the ion species, respectively. Considering that the ion thermal velocity is negligible compared to the large speed of the spacecraft ($\frac{1}{2}m_iv_i^2 \gg k_BT_i$), equation (2) can be expressed as a linear function:

$$I_i = m + bU_{\text{bias}}, \tag{3a}$$

where

$$m \approx \frac{1}{4}A_{LP}q_in_iv_i, \tag{3b}$$

and

$$b \approx A_{LP}q_in_i\frac{q_e}{2m_iv_i}. \tag{3c}$$

During the Grand Finale orbits, v_i was determined by the very fast speed of spacecraft (33–34.5 km/s) near perikrone; therefore, we were able to estimate n_i and m_i using the equations (3b) and (3c). For v_i, we used the spacecraft ram speed of 34.0 km/s. Because of the large inertia of the ions, the ion current was almost linear over the entire bias voltage range and did not become zero when the bias was positive. The ion density was estimated as 524 cm^{-3}, which was slightly (30%) larger than the electron density of 402 cm^{-3}. This result is, to a first approximation, consistent with quasi-neutrality. According to the discussion in Holmberg et al. (2012) on the uncertainty of the ion parameters obtained using this analysis, the error for the ion density value is less than 30% for a density of ~50 cm^{-3} and logarithmically improves as the ion density increases. When the density is >10^3 cm^{-3}, the uncertainty can be <1%. However, the observed current can contain some other effects. This will be discussed in section 4.

In Figure 1, the characteristic mass number expected from this fitting was 1 amu, indicating the predominance of H^+. The orange line shows the current obtained from $H_3{}^+$ ions for comparison. The $H_3{}^+$ density was set to 78.3 cm^{-3}, in accordance with the value obtained by the INMS measurements at the same altitude. The $H_3{}^+$ current gradient was significantly smaller than the H^+ current gradient. This shows that large mass numbers result in smaller current gradients in the negative bias voltages. The black dots are the observed data and the red curves are the fitted total current. There is reasonable agreement at bias voltages up to 0 .1V, where the saturation effect of the electron current started.

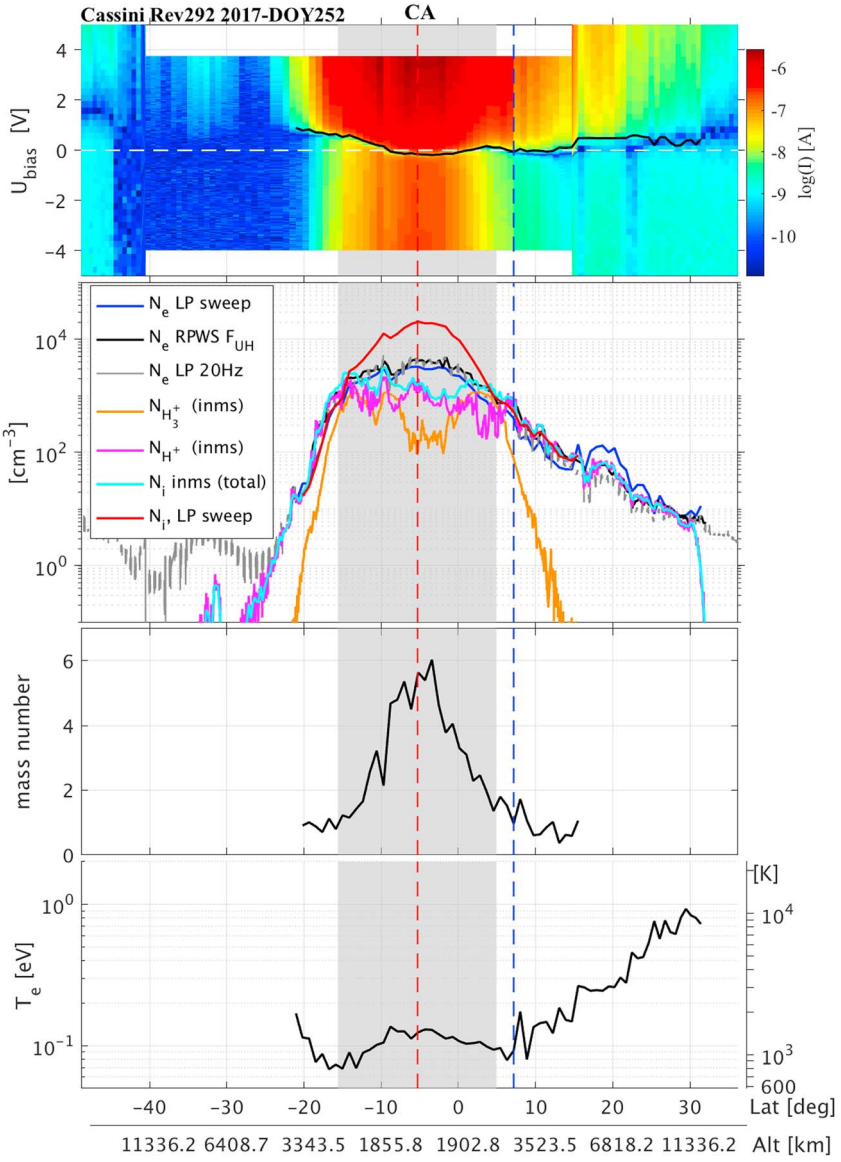

Figure 2. Summary plot of the Cassini/Radio and Plasma Wave Science (RPWS) observation during the Grand Finale orbit 292. (first panel) *I-V* spectrum from the Langmuir probe (LP) observations. The black line shows the negative value of U_{float}. (second panel) The electron and ion densities measured by three different instruments (see legend in upper-left corner). (third panel) Characteristic ion mass number (m_i) in atomic mass unit estimated by the LP. (fourth panel) The electron temperature (T_e) obtained by the LP. The red dashed vertical line over the panels indicates the location of Cassini's closest approach to Saturn. The LP *I-V* curve in Figure 1 was obtained at the location indicated by blue dashed vertical line. The gray-shaded area is where the spacecraft was below 2,500 km. INMS = Ion and Neutral Mass Spectrometer.

3. Overview of Results From the Low-Altitude Orbit 292

Figure 2 summarizes the RPWS and INMS observations obtained during orbit 292 that occurred on 9 September in 2017. Among the 22 Grand Finale orbits, the last five orbits (orbit 288–292) reached especially low altitudes, that is, <3,000 km. All five flybys had nearly identical orbits, which entered Saturn's ionosphere from the north and exited to the south at a local time of ~11.3 hr. The data in Figure 2 are plotted as a function of latitude. The inclination of the trajectory was ~63° and there was a significant north/south asymmetry in the altitude profile, as seen in the *x* axis altitude labels. For example, the spacecraft was at 6,818 km at a latitude of +20°, and it was at 3,343-km altitude when at a latitude of −20°. The

closest approach occurred at 1,685 km in the southern hemisphere at a latitude of −5° (marked with the red vertical dashed lines).

The top panel of Figure 2 shows the *I-V* spectrogram of the LP data. Large currents (red area) were observed around the closest approach in both the positive (electron-attracting side, the "electron current") and the negative (ion-attracting side, the "ion current") bias voltages, indicating the detection of dense ionospheric plasma. The black line in the top panel outlines the negative LP floating potential ($-U_{\mathrm{float}}$). U_{float} is expected to be negative (the black line would be positive in that case) in a cold dense plasma, such as in a planetary ionosphere, but we also observed positive U_{float} values during the Grand Finale orbits. This is discussed later in section 6. The ion and electron densities obtained from the *I-V* characteristics are shown in the second panel of Figure 2. The RPWS was able to estimate the electron density in three different ways (Hadid et al., 2018; Persoon et al., 2018; Wahlund et al., 2017): (1) using the upper hybrid emission (F_{UH}) observed by the RPWS antenna (black line), (2) using the LP continuous mode data (gray line), and (3) using the LP sweep mode data (blue line). These three estimated densities are in good agreement from latitude of −22° to latitude 30°. During the Grand Finale orbits, the electron densities provided by these three different methods agreed with each other through most of the Saturn's ionosphere, which provided confidence in the validity of the electron density measurements. The electron density increased as the spacecraft approached the planet and reached a maximum value of 4.8×10^3 cm^{-3} at closest approach.

The INMS was in the ion detection mode during the orbit 292 flyby and was able to measure the densities of ions of various masses. The magenta line in the second panel of Figure 2 is the ion density of H^+ (mass = 1 amu). The gray-shaded area in Figure 2 is where the spacecraft altitudes became lower than 2,500 km. At high altitudes (outside the shaded area), the H^+ density was almost equal to the electron densities obtained by the RPWS as well as the total ion density obtained by the INMS (cyan line). The LP was also able to estimate the total ion density within −20° < Lat < 15° (red line), and they were consistent with the electron densities and the total ion density obtained by the INMS in this region. The characteristic ion mass estimated by the LP is plotted in the third panel of Figure 2 and inferred to be about 1 amu in the same high-latitude/high-altitude regions. This is consistent with the RPWS observations during the first Grand Finale orbit in the high-altitude ionosphere and shows that Saturn's upper ionosphere is composed of primarily H^+ ions (Wahlund et al., 2017).

When the spacecraft went into the low-altitude (and low latitude within −15° < Lat < 9°) region (gray-shaded area in Figure 2), the $H_3{}^+$ density (orange line) quickly increased while the H^+ density (red line) stops increasing, indicating that the ions with mass > 1 amu, such as $H_3{}^+$, became important. On the other hand, the INMS total ion density (cyan line) did not match the electron densities that were still increasing at low altitudes. Furthermore, the $H_3{}^+$ density decreased as the spacecraft came close to the point of closest approach (−10° < Lat < 0°). Due to Cassini's high speed (~34 km/s), the INMS was not able to measure the heavy ions of mass > 8 amu. The total INMS ion density shown in Figure 2 is the sum of the densities of ions with masses of 1–4 amu. The significant difference between the electron density and the INMS total ion density indicates the presence of the heavier ions (>8 amu), which would, in fact, account for the bulk density of the ionosphere (Waite et al., 2018). Finally, the red line shows the ion density estimated by the LP. Below 2,500 km, the LP-estimated ion density continued to increase as the planet was approached and exceeded the electron density. The total ion density was as high as 2×10^4 cm^{-3}, while the electron density was 3.2×10^3 cm^{-3} and the INMS total ion density was about 2×10^3 cm^{-3}, an order of magnitude lower, at the closest approach. The INMS ion density values include the systematic uncertainty in the detector gain of 21% (Teolis et al., 2015; Waite et al., 2018). The uncertainty of the electron density estimated using f_{UH} is not more than 19% (Persoon et al., 2018). However, because the densities from different instruments (RPWS N_e [F_{UH}], N_e [LP], N_i [LP], and INMS N_i) at high altitude agree with each other within less than ~20%, we are very confident in comparing the observed density values as they are inferred.

The situation where the ion densities are greater than the electron density occurs in other dusty plasma regions such as the E ring (e.g., Wahlund et al., 2009), the Enceladus plume (e.g., Morooka et al., 2011), and the deep atmosphere of Titan (e.g., Shebanits et al., 2013). This situation indicates the presence of negatively charged particles, in addition to the electrons, that serves to provide overall charge balance. The characteristic ion mass estimated by the LP, shown in the third panel of Figure 2, increased near closest approach and reached 6 amu. This mass was derived by assuming that only positive ions contributed to the ion current

in equation (1) and can be seen as a lower bound. If a sufficient number of negative ions contributed, then the average mass would have been larger than the LP-estimated value (Shebanits et al., 2013).

The bottom panel of Figure 2 shows the electron temperature (T_e) obtained by the LP sweep. Two different T_e characteristics can be found depending on the altitude ranges: above 2,500 km (outside the shaded area) and below 2,500 km (shaded area). At high altitudes, T_e gradually increases with increasing altitude (and latitude). This trend is similar to the characteristics obtained during the first Grand Finale orbit (Wahlund et al., 2017). A warmer T_e at high altitudes is often due to the heat inflow from the magnetosphere (Nagy et al., 1976). The lowest T_e values were found to be 0.068 [eV] (788 K) at an altitude of 2,691 km in the northern hemisphere, and 0.078 [eV] (904 K) at an altitude of 2734 km in the southern hemisphere.

On the other hand, in the low-altitude (shaded region), T_e did not continue to decrease toward the planet. Instead, T_e increases and has a maximum near the closest approach (marked as CA in Figure 2 at the red vertical dashed line). This electron temperature enhancement is not consistent with our expectation and it requires a strong local heat source for the ionospheric electrons. At these low altitudes, electron-neutral collisions start to become important and the electron temperature is expected to approach the neutral temperature, which should be below 400 K (Moore et al., 2008). The maximum T_e of ~0.13 [eV] (~1500 [K]) was observed during orbit 292 at an altitude of ~1,700 km.

The validity of the plasma density by the LP is discussed in section 2. In addition to this, the plasma density can be modified around the spacecraft due to the fast speed of the spacecraft body. An electron density enhancement at the foreside of the spacecraft has been recognized near the Earth (Ivchenko et al., 2001), where up to 60% of the density enhancement has been observed. In Saturn's ionosphere condition, the Debye length was 10 cm at most and the spacecraft attitudes were so that the LP directed close to the spacecraft ram. We expect that the LP was well outside the wake formation around the spacecraft. A large speed of neutral can also cause the artificial ionization on the probe surface. However, the kinetic energy of the H_2 at the spacecraft speed (34 km/s) is 12 eV, which is smaller than the ionization threshold of H_2 (15.4 eV). Above all, we emphasize that the electron density measured by the LP has been consistent with the f_{UH} measured, indicating that the plasma disturbances around the probe are not significant. There is also uncertainty in ion density due to the secondary electron to the probe. This will be discussed in the next section.

4. Validity of the LP Ion Measurements

The validity of the electron densities can be confirmed by the consistency of the values estimated using the three different methods discussed above. This validity further confirms that the orbital motion limited concept is still applicable during the observation. Here we discuss the validity of the ion density and mass values estimated from the LP *I-V* sweeps. Figure 3a shows the *I-V* characteristics obtained near the closest approach of orbit 292. At this point, the spacecraft was at 1685 km altitude and latitude −5°. The estimated plasma parameters are given in the left inset in the top panel. The ion density estimated from the fitting was 2.0×10^4 cm^{-3}, which is 6 times larger than the electron density (3.2×10^3 cm^{-3}). The characteristic ion mass obtained was 5.6 amu. Assuming that the measured current was due to only the ram ions, the accuracy of the estimated ion density is ~99% in this region. However, if the LP-measured ion current was affected by anything other than the ambient ions, such as secondary electron currents, the ion density may be overestimated. Here we investigate such an effect. The LP-measured current was the sum of the various currents flowing into and out from the probe:

$$I_{tot} = I_{electron} + I_{ion} + I_{photoelectron} + I_{secondary\ electron} + I_{dust+} + I_{dust-} + \text{etc.} \quad (4)$$

The $I_{photoelectron}$ is the current from the photoelectrons emitted by the LP when exposed to the sunlight. This current appears as a constant value in the negative biased voltages and exponentially decreases to zero for the positive biased voltages. At the distance of Saturn from the Sun, ~9 AU (astronomical unit), the photoelectron current is about 0.5 nA (Holmberg et al., 2012; Jacobsen et al., 2010) and negligible in the dense ionosphere, where I_{ion} is orders of magnitude larger. Any negatively or positively charged dust can create a positive or negative current. Because of the large mass and the large inertia, a dust current affects the analysis of both the ion current and the electron current. However, considering that the validity of the electron density was confirmed by three different measurements, the charged dust current must be negligible.

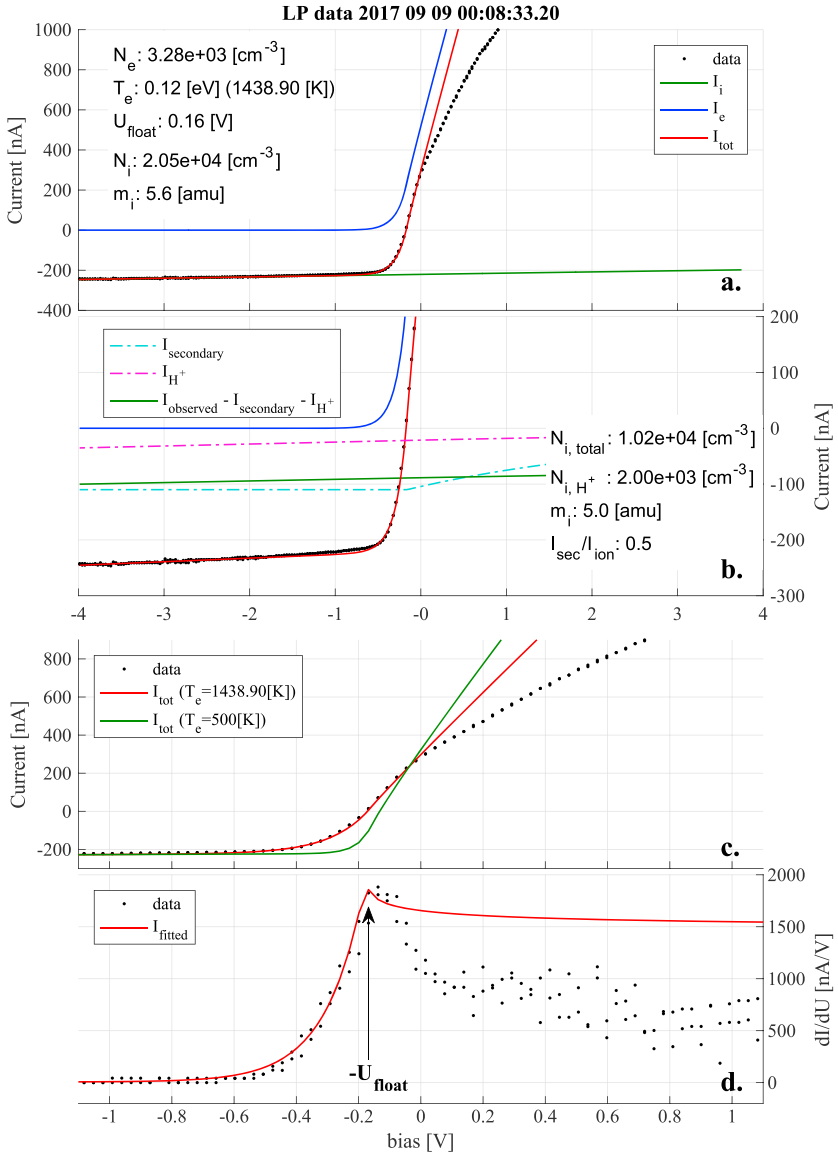

Figure 3. Langmuir probe (LP) *I-V* curve obtained near the closest approach for orbit 292 with different fits. The electron and ion parameters obtained from each fitting are also displayed in an inset in each panel. (a) The original fittings to estimate the electron and ion densities. The blue line is the electron fitting, the green is the ion, and the red is the sum of the fitted ion and electron currents. (b) The *I-V* fitting with secondary electron current (cyan dashed dot line). The H^+ ion current (magenta dashed dot line) is included. $I_{\text{measured}}-I_{\text{secondary}}-I_{H^+}$ (green line) is therefore regarded as the current carried by the heavy ions. (c) Same fitting as Figure 3a, but the bias voltage area is enlarged to ±1 [V]. The green line is the theoretical curve with the colder electron temperature (500 [K]). (d) The first derivative of the observed current (black dots) and the fitted current (red line) from Figure 3c. The peak of the first derivative is used to identify the probe floating potential (marked with an arrow).

When a LP probe is immersed in a certain type of superthermal particle plasma, it can emit secondary electrons. With respect to Cassini's LP, this secondary electron current is sensitive to electrons with energies of 250–450 eV (Garnier et al., 2012). We assume that the secondary-electron current is similar to the photoelectron current and investigate the effect of secondary electrons on our ion current analysis. Figure 3b shows the data fit with the assumption that half of the ion current was caused by the secondary-electron current. We also included the contribution to the current by the H^+ ions (magenta line) using the H^+ density value from the INMS (2.0×10^3 cm^{-3}). Thus, the rest of the current, $I_{\text{observed}}-I_{\text{secondary}}-I_{H^+}$ (green line), is the current from the heavier ions. This analysis results in a total ion density of 1.02×10^4 cm^{-3} and shows that even

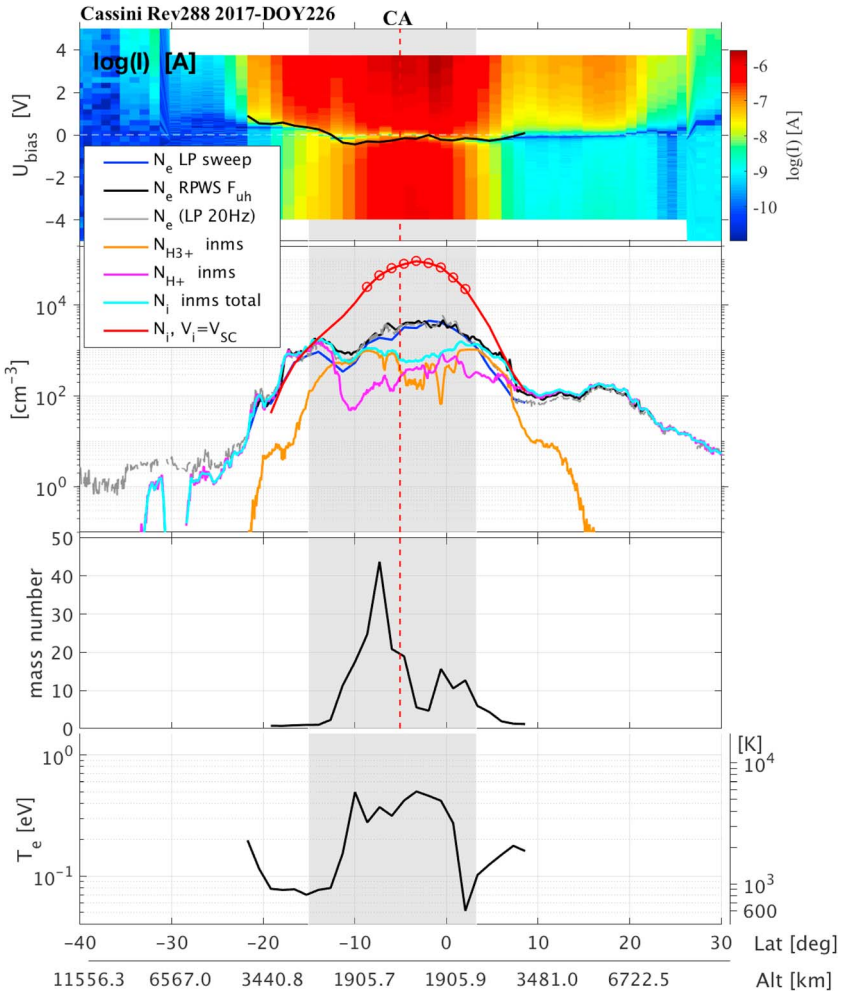

Figure 4. Summary plot of the Cassini/Radio and Plasma Wave Science (RPWS) observations during the Grand Finale orbit 288. The plot format is the same as that used in Figure 2. INMS = Ion and Neutral Mass Spectrometer.

if a large secondary current is included, only 20% of the total ion density is attributed to H^+. On the other hand, the characteristic ion mass of 5.0 amu is still smaller than the 8 amu expected from the INMS observation (Waite et al., 2018). The increasing of the secondary current results in the reduction of the *m* value in equation (3a). This causes the reduction of the ion density in equation (3b) and further decreases the ion mass value in equation (3c) as well. In order to keep a large ion mass number that is consistent with the INMS result, the secondary-electron current must be smaller than the value we used here, so the error in the ion density cannot be more than 10%.

5. "Unusual" *I-V* Characteristic Obtained During Rev 288

During the Grand Finale orbits, the Cassini LP observed electron and ion density discrepancies at altitudes below 2,400 km, where instruments onboard Cassini indicated the presence of small dust grains and heavy organic molecules (Mitchell et al., 2018; Waite et al., 2018). In the dusty plasma region of the Earth's mesosphere, the kinetic impact of heavy cluster molecules on the surface can fragment the clusters and produce positive and negative ions. During one of the low-altitude flybys of the Grand Finale, the Cassini LP obtained the *I-V* curves, possibly resulting from the impact of the kinetic clusters. In this section we describe the general electron density analysis method of the Cassini LP and the special *I-V* curves observed at low altitudes in Saturn's ionosphere.

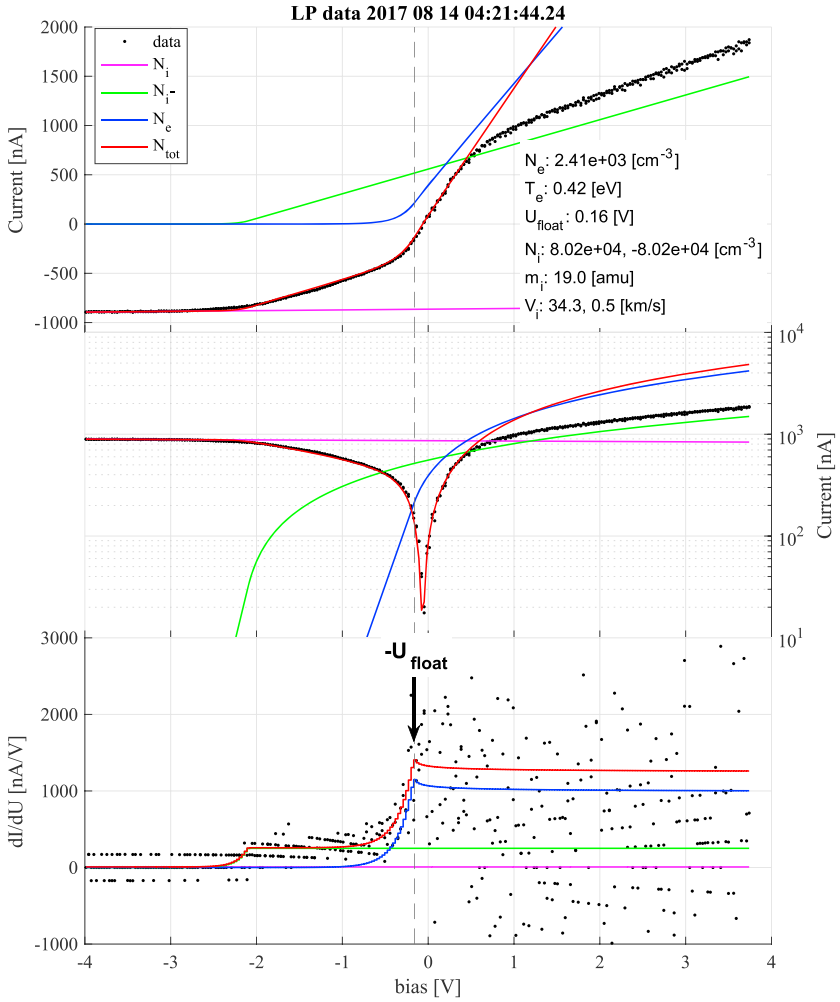

Figure 5. Example of a Langmuir probe (LP) *I-V* curve during orbit 288. The plot format is the same as that used for Figure 1 in the main text. The black dots are the observed current and the solid lines show the modeled current for the different species: magenta for the positive ion, green for the negative ion, blue for the electron, and red for the sum of ions and the electrons. The fitted parameters are given on the left inset in the top panel.

Figure 4 shows the summary of the orbit 288 observation in the same format as Figure 2. The ion and electron densities are shown in the middle panel. The general characteristics of the density structure are similar to those observed during orbit 292, described in section 3: (1) The electron and ion densities were enhanced around the closest approach, which occurred at approximately −5° latitude. (2) The observed ion density was significantly higher than the electron density. Comparison between the INMS and the RPWS observations showed that the lighter-mass ion density (< 4 amu, cyan line) was smaller than the electron densities, indicating the presence and dominance of the heavier ions in the ionosphere. (3) The ion mass estimated by the LP (the third panel in Figure 4) also showed an increase in mass number around closest approach. The ion densities obtained during this event were somewhat higher than the values obtained during the other flybys. The peak ion density of 9.3×10^4 cm^{-3} was twice as large as the ion densities from the other flybys, which were typically up to 5.0×10^4 cm^3, twice the typical value.

Figure 5 is the LP *I-V* curve obtained at the closest approach point (red vertical dashed line in Figure 4) during Rev 288. This *I-V* characteristic is clearly different from those for the two other observations shown in Figures 1 and 3 in that an extra current appeared in the bias voltage range -2 V $< U < -0.5$ V in addition to the usual positive ion (magenta) and the electron (blue) currents. The velocity of the positive ion (V_i) was set to 34 km/s, which is consistent with the spacecraft ram velocity. On the other hand, the additional current (green) was characterized by the negatively charged ions with a potential at +2 V relative to the

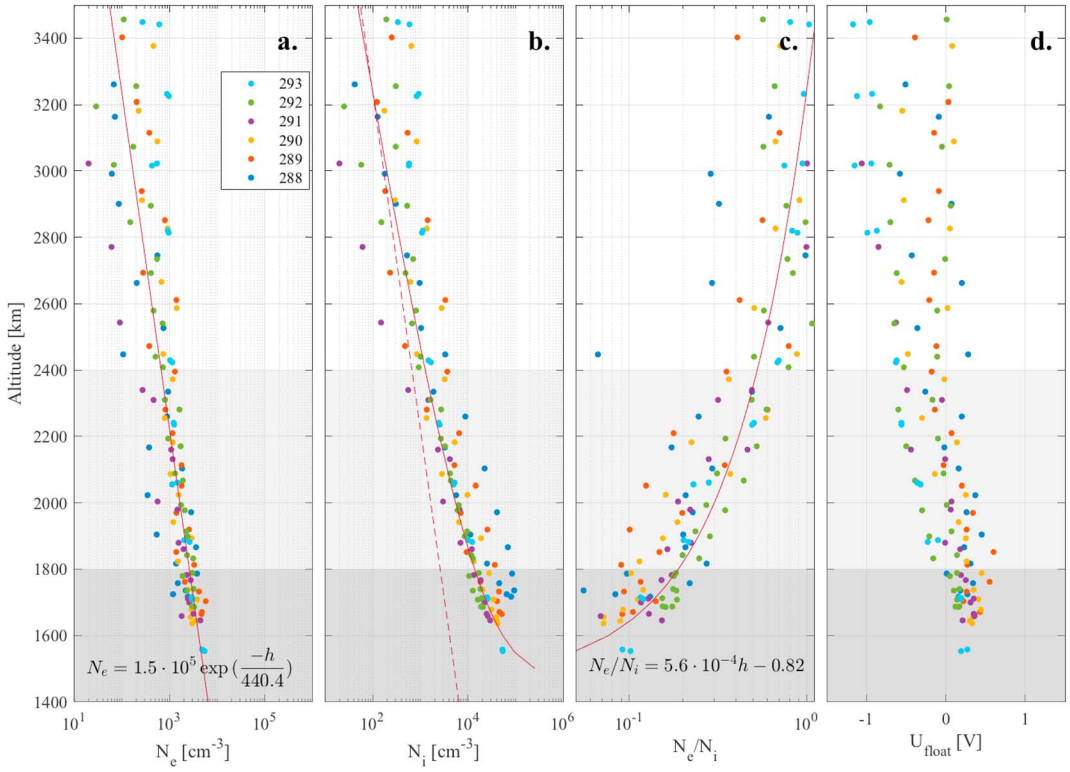

Figure 6. Altitude profiles of the plasma parameters estimated by the Langmuir probe during the low-altitude orbits of the Grand Finale (288 to 293). (a) Electron densities. The solid line is the profile fitted to the function displayed at the bottom of the panel. (b) Ion densities. The dashed line is the fitted electron profile obtained in panel (a), and the solid line is the fitted ion density profile resulting from the functions shown at the bottom of (a) and (c). (c) Electron density to ion density ratio. All the data (excluding that of orbit 288 because of the heavy ion impact effect) were fitted to the linear function displayed at the bottom of the panel. (d) Floating potential of the Langmuir probe. Light shaded areas indicate the region where N_e/N_i departs from 1 by more than 30%. $U_{float} > 0$ was observed for all flybys at altitudes below 1,800 km (dark shaded area).

probe and very small velocity (0.5 km/s). The ion mass (m_i) is set to 19 amu for both positive and negative ions in this fit. As a result, the total current (red) matches the observed current (black) very well. The slow speed of the negative ion implies that they are traveling with spacecraft as if they have just been created around the LP sensor. We interpret that the extra current is a result of cluster fragmentation and ionization occurred on the probe surface and that the extra negative ions were created and surrounded the probe. This is similar to what has been observed in the noctilucent clouds and the polar mesospheric summer echoes layers in the Earth's mesosphere (Havnes et al., 2009) and in laboratory experiments (Andersson & Pettersson, 1997; Tomsic et al., 2000 ; Vostrikov et al., 1997). The floating potential of the probe (U_{float}) was +0.16 V, which can be identified by a kink in the electron current gradient (see the bottom panel). This value was used to fit the electron and the positive ions.

This type LP *I-V* curve can be regarded as evidence of cluster molecules in Saturn's ionosphere. However, this clear indication of the negative ions was obtained only during Rev 288 and possibly only one sweep near the closest approach of Rev 289. The secondary-electron effect on dust was not present for the rest of the observations. The scattering of cluster molecules on the probe surface depends on the size and speed of the molecules as well as on the inclination of the incoming flux with respect to the surface (Tomsic et al., 2000; Vostrikov et al., 1997). The appearance of the negative ion current in the LP *I-V* curve can be related to the variability in particle sizes or in the velocity of neutrals from orbit to orbit.

6. Ionospheric Density Characteristics From All the Low-Altitude Flybys

In section 3, we presented the LP observations of the electron and ion densities from orbit 292, one of the last five Grand Finale orbits, which reached an altitude below 3000 km. The observed characteristics from that

orbit are applicable to the other four low-altitude orbits. Figure 6 shows the altitude profiles of all of the LP-estimated parameters of the last five orbits (orbits 288–292) and Cassini's final plunge (orbit 293). Figure 6a shows the electron densities N_e. The solid line is the fit of all the electron density data to the function

$$N_e = n_0 \exp\left(-\frac{h}{H}\right) \tag{5}$$

where h is the altitude, n_0 is the maximum density at altitude 0 km, and H is the scale height. The fit yielded $n_0 = 1.5 \times 10^5$ cm^{-3} and $H = 440.4$ km. Most of the data points are within 50% of the fitted line at low altitudes below 2000 km, while they are more scattered and show larger variability in N_e from orbit to orbit at higher altitudes. The scale height obtained here can be compared to the values obtained by Hadid et al. (2018). Their values in the northern hemisphere were 840 km at the middle altitudes (<4,000 km) and 260 km at the low altitudes (<2,200 km). Our scale height (440.4 km) is consistent. Figure 6b is the ion densities N_i, with the dashed line the fitted electron density profile from Figure 6a. The ion densities also increased with decreasing altitudes, but the trend clearly deviated from that of the electron density below 3,000 km. Figure 6c shows the ratio of electron density to ion density (N_e/N_i), which gradually falls from 1 at an altitude of 3,000 km to 0.1 at around 1,700 km. The solid line is the fit of N_e/N_i to the linear function $N_e/N_i = 5.6 \times 10^{-4}\, h - 0.82$ versus altitude. The solid line in Figure 6b is the ion density derived from the fitted N_e profile in Figure 6a and the fitted N_e/N_i profile in Figure 6c. Because there is some uncertainty in the LP sweep density measurements (30% in N_e, see section 2, and 10% in N_i), N_e/N_i probably departs from 1 by more than 30% at altitudes below 2400 km (light shaded area). A small N_e/N_i ratio indicates the presence of a dusty plasma and a reduction in the electron densities can be expected. This might explain why the previously observed electron densities (Kliore et al., 1980, 2009; Nagy et al., 2006) were lower than those expected from the model (e.g., McElroy, 1973).

Figure 6d shows the altitude profile of the LP floating potential U_{float}. When a dust grain is immersed into a dense and cold space plasma it attaches surrounding mobile electrons and its potential becomes usually negative (e.g., Horanyi, 1996). In space, the LP acts like the dust grains in space. Since the observed N_e/N_i ratio was small, U_{float} should have been negative, and indeed, the observed U_{float} was mostly negative above 2,000 km. However, as the N_e/N_i ratio decreased at lower altitudes, U_{float} continued to increase and turned positive below 2,000 km. In fact, positive U_{float} was observed in all flybys below 1,800 km (dark shaded area). The positive U_{float} can be clearly seen in the *I-V* curve obtained near the closest approach (Figure 3d). A current gradient peak occurred at $U = -0.16$ V, so that $U_{\mathrm{float}} = +0.16$ V.

One possible explanation for the positive U_{float} is the effect of secondary electrons due to the high-energy electron impact. However, we have estimated that the secondary electron effect should be <10% and thus is unlikely to cause a positive U_{float}. Another cause of the positive U_{float} could be the modification of the *I-V* curve due to a strong magnetic field (e.g., Bohm et al., 1949). During the Grand Finale, Cassini was in a strong magnetic field ($B \sim 2 \times 10^4$ nT). Such an effect by the magnetic field has been observed above the Earth's ionosphere within a tenuous plasma in the auroral particle acceleration region (Hilgers et al., 1992). In such cases, the LP-emitted photoelectrons, which were efficiently trapped within the magnetic flux tube resulting in a photoelectron current, could lead to a positive spacecraft potential. However, this effect applies only to tenuous plasma regions. Considering the validity of the electron density from the three independent measurements, the effect must be negligible.

The secondary-electron emission from the impact of dust may not be negligible (Havnes et al., 2015), and the secondary-electron current can result in a positive U_{float}. The impact of the kinetic neutral clusters on the solid surface causes fragmentation of the cluster and produces secondary-electron emission resulting in pairs of negatively and positively charged ions. A large secondary-electron flux emitted by the probe can result in a positive U_{float}. The signature of the heavy negative and positive ions has actually been observed in the ionosphere by the LP (see section 5). However, this type of observation was a special case and occurred only during orbit 288 and possibly in one sweep in orbit 289. On the other hand, these events indicate the presence of the heavy cluster molecules in Saturn's ionosphere.

Finally, we consider that the observed positive U_{float} is a result of the composition of the plasma in Saturn's ionosphere. Laboratory experiments (e.g., Kim & Merlino, 2006) showed that the dust grains can have

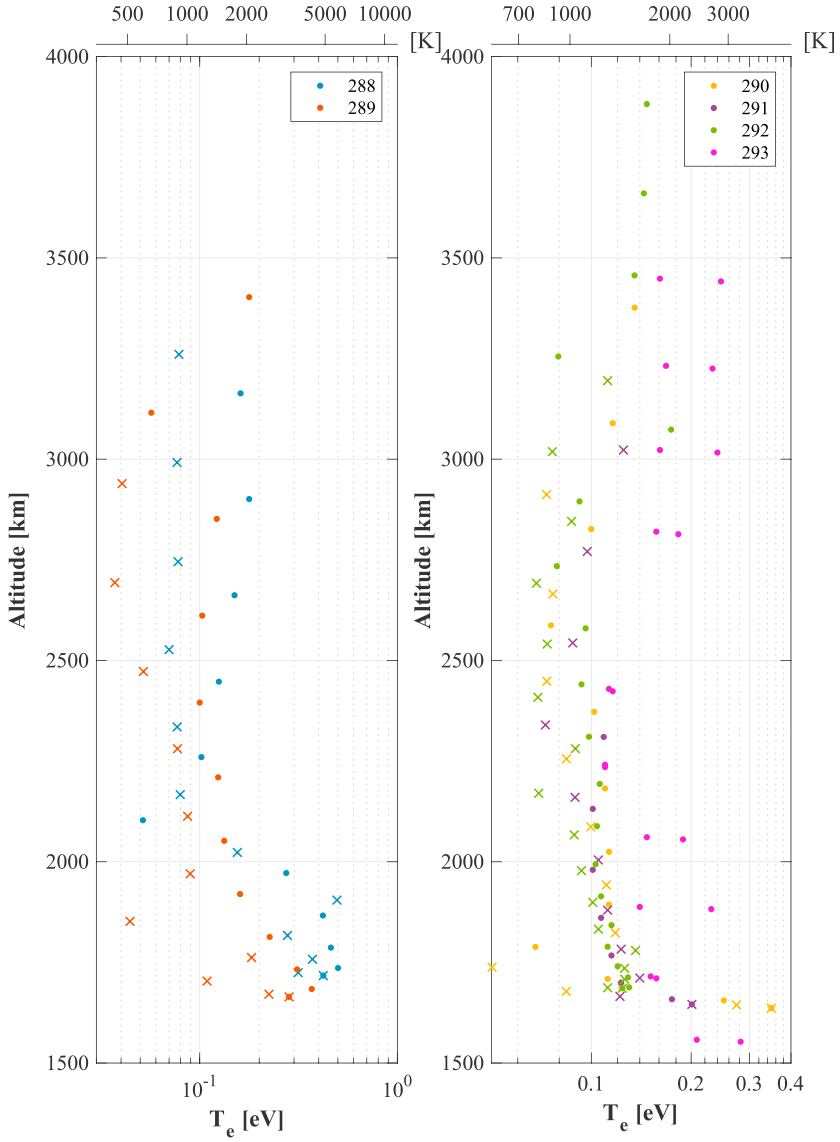

Figure 7. The altitude profile of the electron temperature obtained for orbits 288–289 (left) and orbits 290–293 (right). Each orbit is plotted in a different color (see the legend in each panel). The dot marks are from inbound (northern hemisphere) data and the cross marks are from outbound (southern hemisphere) data.

positive potential when the surrounding plasma is composed of electrons, positively charged ions, and negatively charged ions. The theory is that if the concentration of the negative ions, with larger mass than the positive ions, is comparable to that of the positive ions, the light positive ions will be the most mobile in the system and the dust grains will acquire a positive charge. Because the LP is like an isolated grain in the surrounding plasma, the positive U_{float} in the region where the electron and ion densities are unequal is consistent with an ionosphere consisting primarily of heavy positive and negative ions.

7. The Electron Temperature in the Low-Altitude Ionosphere

Figure 7 shows the altitude profile of the electron temperature (T_e) obtained from all the low-altitude orbits (orbits 288–292) and the final plunge (orbit 293). These orbits occurred every ~6.45 days and the T_e intensity range changed during the five observation periods. Therefore, the profiles are plotted separately in two groups: the first two orbits (left panel) and the later four orbits (right panel). Two different markers differentiate the inbound (dot) and outbound (cross) data. In section 2 the in situ electron temperature

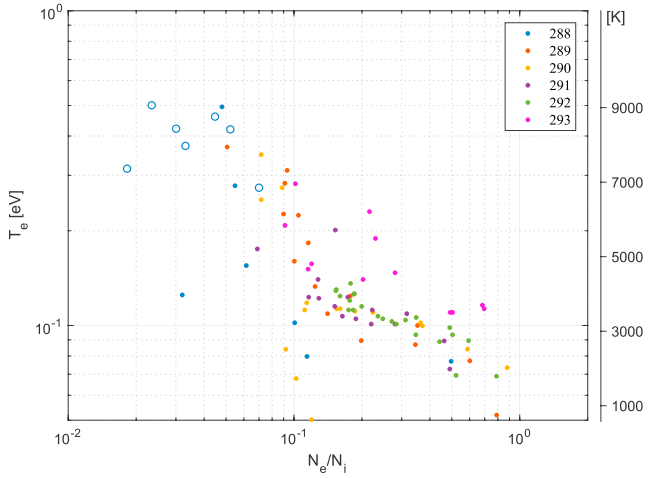

Figure 8. The relationship between the electron temperature (T_e) and the electron to ion density ratio (N_e/N_i) obtained below the altitude of 2,500 km for all low-altitude flybys (orbits 288–293).

measurement in the low-altitude ionosphere of Saturn has been presented, showing two different electron temperature characteristics which were dependent on the altitude range: above and below 2,500 km.

Above 2,500-km altitude, a trend showing T_e increasing with increasing altitude can be found. During orbit 292 (Figure 2) T_e reached the highest value of 10^4 [K] at an altitude of ~11,000 km. The minimum T_e values are usually found to be ~0.08 eV (~700 [K]) around 2,500 km. During the first two orbits (left panel), the temperature gradient at high altitudes is less pronounced. Heat transport by the magnetospheric plasma is commonly observed in the planetary ionospheres and moons (Edberg et al., 2010; Hoegy et al., 1980; McDonald & Williams, 1986; Nagy et al., 1976). In the ionospheric model by Sakai and Watanabe (2016) the electron temperature T_e was found to be heated up to 10^4 [K] at an altitude of 5,000 km due to the heat flow from the magnetospheric electrons with energy of 2 eV. This value is much larger than the observed value (~1500 K), and it requires less energy input via heat conduction from the magnetosphere to be consistent with our observation. Since Sakai and Watanabe (2016) considers the ionosphere in the middle latitude (~50°), different temperature of the magnetospheric electrons in different L shell can exist here. In the left panel, the outbound temperatures (dots) seem to be ~0.05 eV warmer than the inbound temperatures (crosses). This may indicate the heat source differences depending on different L shell (L shell ranges for inbound were ~1.02, while they were ~1.05 fore outbound. See Figure 10), however, such differences were not clear for the other orbits (right panel).

At low altitudes below 2,500 km, a strong electron heating process takes place, which gives rise to observed electron temperatures up to 5000 K in the altitude range of 1,400 to 2,000 km. An electron temperature increase of about 500 K is actually expected in the model by Moore et al. (2008) on the dayside near the plasma density peak, assuming only solar EUV ionization heating, which is most effective in the altitude range 1,200–2,000 km. Below 1,200 km the electron-neutral collision is too large and temperatures need to be cooled down to 150 K at most. Obviously, the electron heating by the solar EUV ionization of neutrals cannot explain the observed electron temperature by RPWS/LP reported here. Instead, an electron heat source that gives electron temperatures about 1 order of magnitude larger is required.

The electron heating found at low altitudes did not show a clear relationship with altitude. The T_e maximum occurs not at periapsis, but often just above the periapsis. In Figure 2, we found also that the low-altitude T_e enhancement was associated with the region where the ion density exceeds the electron density. Figure 8 shows the relationship between T_e and the electron to ion density ratio (N_e/N_i) below 2,500 km for the low-altitude orbits. A clear trend showing T_e increasing with decreasing N_e/N_i can be identified. The blue circles are special cases obtained during orbit 288, where unusual *I-V* curves, which could be a result of the kinetic negatively charged ions caused by the kinetic cluster molecules impact, occurred (*see* section 5). The ion density of these cases can be overestimated by a factor of ~2, and the data points can then be shifted toward the right (toward larger N_e/N_i). However, we believe these negatively charged kinetic ions do not affect the electron temperature estimate, as they are heavy and cannot give rise to an exponential electron feature from which the electron temperature is directly measured.

The correlation between the T_e and N_e/N_i obtained here implies that the electron heating process may be related to the dusty plasma state. A similar increase in the T_e was reported in the Janus/Epimetheus rings (Morooka et al., 2018) and indicated in the dusty ionosphere of Titan (see review by Galand et al., 2014). The observed electron temperature increase can be due to many processes. If dust grains absorb and remove a large number of cold electrons from the ambient plasma, it can cause a "filtration" effect such that the observed temperature are of the higher energy electron component. High concentration of negatively charged dust may cause electron acceleration within their potential wells (Farrell et al., 2017). Energy deposition may also be the result of a nanometer-sized particle from the D ring (Hamil et al., 2018; Mitchell et al., 2018), where at low altitudes the nanometer-sized grains impact the atmosphere, break apart and sublimate, slow down, and accumulate near the ionospheric peak. Last, the dust grains are illuminated

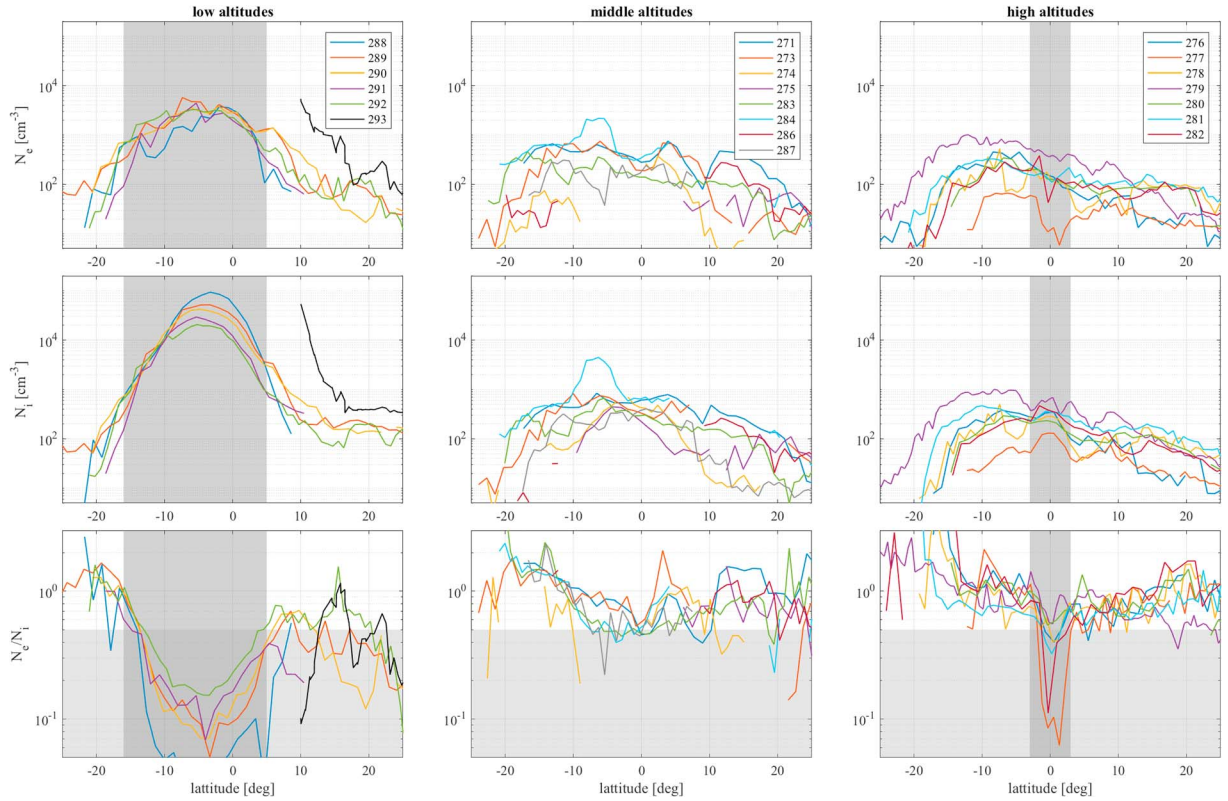

Figure 9. The electron and ion densities obtained by the Langmuir probe sweep during the Grand Finale orbits. The latitudinal profiles of the electron (top row) and ion (middle row) densities and the N_e/N_i ratio (bottom row) for each orbit are shown in three different altitude ranges. In the bottom panels, the horizontal lightly shaded area is where the N_e/N_i ratio is less than 0.5 and is expected to be dusty. The vertical darkly shaded areas for the low-altitude and the high-altitude orbits are where the N_e/N_i ratio were significantly small.

by the solar EUV radiation and subject to photoelectron emissions with energies of about 2 eV. These thermalize quickly through collisions with the ambient thermal ionospheric electrons and the electron temperature rises. Extra warm electrons are often been found in addition to photoelectrons in the Enceladus plume (Coates et al., 2013). Moore et al. (2008) estimated the electron temperature in considering the heating by the photoelectron produced from the neutral ionization and showed the local temperature enhancement up to 500 [K] under the sunlit condition. By including the extra electron, detachment from grains by EUV into this model will cause extra the electron heating. In any case, the observed electron temperature by the RPWS/LP significantly affects the recombination rates in the ionosphere of Saturn, which needs to be considered by ionospheric models.

8. Summary and Discussion

We presented the LP measurements of ion and electron densities in Saturn's ionosphere obtained during Cassini's Grand Finale orbits. The low-altitude observations consistently showed a rapid increase in plasma densities as the spacecraft approached the planet and discrepancies between the electron and ion densities below 2,500 km. The ratio of electron density to ion density gradually decreased with decreasing altitude until it was <0.1 at ~1,700 km. The small ratio indicates the presence of a dusty plasma, that is, a plasma consisting of electrons, ions, and negatively charged grains. Contrary to the expectation that the electrical potential of the dust is negative in a cold and dense plasma, the LP U_{float} turned into positive in the region where the electron and ion densities are unequal. We interpreted that the positive LP U_{float} occurring in Saturn's dusty ionosphere as evidence of negatively and positively charged heavy ions and electrons.

During the Grand Finale orbits, the Cassini's instruments found evidence of nanometer-sized D ring dust grains. The Magnetospheric Imaging Instrument observed particles in the energy range from about 40 to

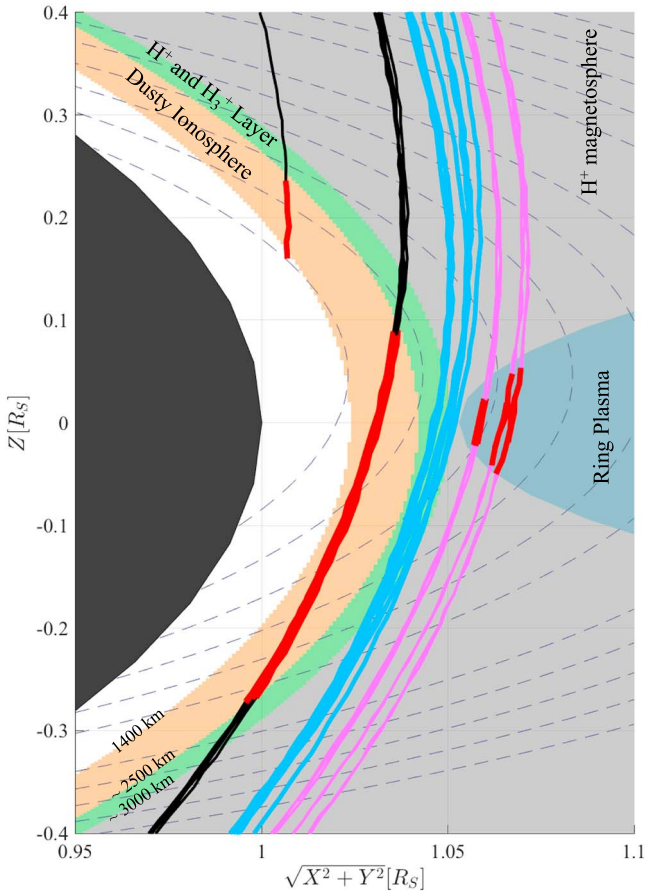

Figure 10. The schematic picture of the charged dust region based on this study. Solid lines are the Cassini trajectories in the Kronian Equatorial coordinate system (Z is the planet spin axis; X and Y are in the equator plane) for each of the altitude ranges (black for the low altitudes, blue for the middle altitudes, and pink for the high altitudes). The thick red lines show where the negatively charged dust exists. The background colors represent the different plasma characteristics based on the result from Figure 9. Below 2,-500 km altitudes the dusty ionosphere can be detected. The layer of H_+ and H_3^+ mixed upper ionosphere can be found between the altitudes of 2,500 and 3,000 km. The high altitudes orbits path through the D ring at the equator.

220 keV that corresponds to 15,000–40,000-amu mass particles near the D ring at ~3,000-km altitude, with the positively charged component of these particles in the ionosphere at ~1,700–2,000 km (Mitchell et al., 2018). The INMS has observed various heavy organic components of neutrals. The heavy neutrals up to 78 amu have been detected from the low altitudes of 1,500 km to the high altitude at 3,500 km near the D ring, implying the particle inflow into the ionosphere from the D ring (Waite et al., 2018). The D ring grains collide with atmospheric constituents and can fall under the pull of gravity (Mitchell et al., 2018). Signatures of the negatively charged dust in the D ring were also observed by the LP (Wahlund et al., 2017) that were associated with submicrometer-sized dust impacts (Ye et al., 2018).

Figure 9 shows the electron and ion density observations from the LP sweep during the Grand Finale orbits. The latitudinal profiles of the electron (top three panels) and ion (middle three panels) densities and their ratio (lowest three panels) for each orbit are shown in three different altitude ranges. The LP was able to obtain the sweep data overall with good coverage during the Grand Finale orbits. However, both electron and ion densities were underestimated when the probe was situated in the wake of the spacecraft. The wake effect occurred in Rev 272, Rev 285, and a part of Rev 273 and 284. The electron density was underestimated also when the electron temperature was large compare to the LP's maximum bias voltage (4 V). The high-energy electron temperature effects happened especially at higher altitudes and were found during short time intervals in Rev 275, 279, and 286. These data points are excluded from Figure 9. The low-altitude orbits (the left panels) are from the last five flybys (Rev 288–292) and the final plunge (Rev 293) and are the same data set as Figure 6. Density enhancements were observed near the equator in both electron and ion and the density peaks were tilted toward south about −5°. This density peak locations correspond to the closest approaches. The horizontal dark shaded area is where the spacecraft was below an altitude of 2,500 km and where the ion density deviated from the electron density for Rev-292 (dark shaded area in Figure 2). The vertically light shaded area is where the N_e/N_i ratio becomes <0.5, and the small N_e/N_i ratio has been located within −16° < Lat < 5° in the low-altitude orbits. The high-altitude orbits (the right panels) occurred during Rev 276–282 and their closest approaches were located above 3,000 km. The density trends of the electrons and ions densities are similar in that they gradually increase with decreasing latitude and reach peak around −10° latitude. In a small region at the equator (vertically dark shaded area), decreasing densities for the electrons and density enhancements for the ions, respectively, can be found for some of the orbits. It is clear that these electron density decreases and ion density increases result in the decreasing of the N_e/N_i ratio in the bottom panel. The small N_e/N_i ratio was clear especially during Rev 277 and 282, where the spacecraft trajectories were at the highest altitudes among the Grand Finale orbits. During the ring crossing of the high-altitude orbits the micrometer-sized dust grains were detected by the RPWS antenna. The observed dust density existed in a narrow (±500 km from the equator) region and orders of magnitude lower than the dust density obtained during the Dust Grazing orbit just outside the F ring (Ye et al., 2018). Comparison between the dust density by the RPWS antenna and the charged density from the LP is consistent with most of the negative charge being carried by smaller sized grains ranging from tens of nanometers to submicrometers. It must be pointed out that the large-scale density peaks are not located at closest approach (located around −5° latitude) but slightly southward near −10° latitude. During the middle-altitude orbits (Rev 271–275 and Rev 283–287) closest approach ranged from 2,600 to 3000 km (middle panels). The densities in the middle-altitude orbits were highly variable and the density maximums are located around −5° latitude. There

was no significant difference in electron and ion densities and, as one sees in the middle-bottom panel, N_e/N_i ratio had not significantly decreased. Therefore, we conclude that the number of charged grains were small in the middle altitude orbits.

Figure 10 is a schematic picture of the charged dust region based on the results of Figure 9. Solid lines are the Cassini trajectories in the Kronian Equatorial coordinate system (Z is the planet spin axis, X and Y are in the equator plane) for each altitude ranges (black for the low altitudes, blue for the middle altitudes, and magenta for the high altitudes). The thick red lines show where negatively charged dust exists. This is defined by altitudes below 2500 km for the low-altitude orbits, by latitudes within ±3° of the equator plane for the outer high-altitude orbits (Rev 277 and 282) and by latitudes within ±1.5° of the equatorial plane for the rest of the high-altitude orbits. The background colors represent the different plasma characteristics. The LP observed small N_e/N_i ratios indicating the presence of negative charged grains in two regions: at low altitudes below 2,500 km and in a narrow region of the equator at high altitudes above 3,000 km. Both regions are dusty, the dust and plasma are in collective ensemble, but are different in characteristic dust sizes. At low altitudes dust grains are on the order of a nanometer or less, comparable to cluster ions, while dust in the high altitudes are larger, tens of nanometers to submicrometers. Just above the dusty ionosphere, the plasma components are predominantly H^+ with a significant H_3^+ component. A significant amount of H_3^+ was also observed in the middle-altitude orbits associated with the closest approach (Waite et al., 2018). Beyond the H^+ and H_3^+ layer, the plasma is dominated by H^+ except near the ring at the equator.

In our study, the LP revealed the dusty plasma state of the ionospheric plasma from which a dominant component of negatively charged by heavy ions was inferred. We confirmed the presence of the charged dust in the planetary ring above Saturn's ionosphere. These observations indicate a new scenario for ring rain, whereby the small particles from the D ring precipitate into the ionosphere possibly changing its chemistry into the dusty negative ion plasma that we observed. While heavy neutrals have been detected consistently from low altitudes to high altitudes in the ring (Waite et al., 2018), the LP observation did not show a significant signature of the charged grains at the middle altitudes between the ionosphere and the ring.

In the terrestrial atmosphere the layers of metal atoms exist as a result of meteoric ablation. These metal atoms become the condensation nuclei of the ice particle that are observed as the noctilucent cloud, where in dusty plasma characteristics are often observed (e.g., Havnes, 2002). Cassini observations from the Grand Finale, including this study, show that the inflow of the water particles from the D ring into the atmosphere of Saturn. The precipitating nanometer-sized ice dust of the “ring rain” chemically interact with the upper ionosphere create the layer of H^+ and H_3^+, further undergo sublimation and fragmentation when they impact the deeper atmospheric layers. Grains on the order of 1–10 nm deposit their energy in the altitude range of 1,700–1,900 km, and the accumulation of such particles may form a grain-rich layer in the atmosphere (Hamil et al., 2018). The observations in this study indicated that dusty plasma effect that are observed in the terrestrial mesosphere can exist permanently in the equator region of Saturn's upper atmosphere. Investigation of the dust falling process including the grain charge and chemical processes will be further needed to understand Saturn's dusty ionosphere of heavy ions detected by the Cassini measurements.

Acknowledgments
The authors acknowledge funding and RPWS/LP instrument support by the Swedish National Space Board, and the Cassini project support by NASA. M. W. M., N. J. T. E., D. J. A., and L. Z. H. acknowledge funding by the Swedish National Space Board under contracts Dnr 174/15, 135/13, and 162/14, respectively. N. J. T. E. and L. Z. H. also acknowledge funding VR under contracts 621-2013-4191 and 2.2.1-312/16, respectively. The research at the University of Iowa was supported by NASA through contract 1415150 with the Jet Propulsion Laboratory. The INMS team is supported by the Cassini INMS subcontract from NASA with JPL (NASA contract NAS703001TO NMO711123, JPL subcontract 1405853); and INMS science support grant NNX13AG63G (M. E. P.). Cassini RPWS data will be available at the NASA Planetary Data System (https://pds.jpl.nasa.gov). Author would like to thank *Editage* (www.editage.jp) for language support.

References

Andersson, P. U., & Pettersson, J. B. C. (1997). Z Phys D—Atoms. *Molecules and Clusters*, *41*(1), 57–62. https://doi.org/10.1007/s004600050289

Bohm, D., Burhop, E. H., & Massey, H. S. (1949). *The characteristics of electrical discharges in magnetic fields*. New York: McGraw–Hill.

Coates, A. J., Wellbrock, A., Jones, G. H., Waite, J. H., Schippers, P., Thomsen, M. F., et al. (2013). Photoelectrons in the Enceladus plume. *Journal of Geophysical Research: Space Physics*, *118*, 5099–5108. https://doi.org/10.1002/jgra.50495

Connerney, J. E. P., & Waite, J. H. (1984). New model of Saturn's ionosphere with an influx of water from the rings. *Nature*, *312*(5990), 136–138. https://doi.org/10.1038/312136a0

Cravens, T. E., Moore, L., Waite, J. H., Jr, Perryman, R., Perry, M., Wahlund, J.-E., et al. (2018). The Ion Composition of Saturn's Equatorial Ionosphere as Observed by Cassini. *Geophysical Research Letters*, *45*. https://doi.org/10.1029/2018GL077868

Edberg, N. J. T., Wahlund, J.-E., Ågren, K., Morooka, M. W., Modolo, R., Bertucci, C. L., & Dougherty, M. K. (2010). Electron density and temperature measurements in the cold plasma environment of Titan: Implications for atmospheric escape. *Geophysical Research Letters*, *37*, L20105. https://doi.org/10.1029/2010GL044544

Fahleson, U. (1967). Theory of electric field measurements conducted in the magnetosphere with electric probes. *Space Science Reviews*, *7*(2–3), 238–262. https://doi.org/10.1007/BF00215600

Farrell, W. M., Wahlund, J.-E., Morooka, M. W., Kurth, W. S., Gurnett, D. A., & MacDowall, R. J. (2017). Ion trapping by dust grains: Simulation applications to the Enceladus plume. *Journal of Geophysical Research: Planets*, *122*, 729–743. https://doi.org/10.1002/2016JE005235

Galand, M., Coates, A., Cravens, T., & Wahlund, J. (2014). Titan's ionosphere. In I. Müller-Wodarg, C. Griffith, E. Lellouch, & T. Cravens (Eds.), *Titan: Interior, Surface, Atmosphere, and Space Environment, Cambridge Planetary Science* (pp. 376–418). Cambridge: Cambridge University Press. htttps://doi.org/10.1017/CBO9780511667398.014

Garnier, P., Wahlund, J.-E., Holmberg, M. K. G., Morooka, M. W., Grimald, S., Eriksson, A., et al. (2012). The detection of energetic electrons with the Cassini Langmuir probe at Saturn. *Journal of Geophysical Research*, *117*, A10202. https://doi.org/10.1029/2011JA017298

Gurnett, D. A., Kurth, W. S., Kirchner, D., Hospodarsky, G., Averkarnp, T. F., Zarka, P., et al. (2004). The Cassini radio and plasma wave investigation. *Space Science Reviews*, *114*(1–4), 395–463. https://doi.org/10.1007/s11214-004-1434-0

Gustafsson, G., & Wahlund, J.-E. (2010). Electron temperatures in Saturn's plasma disc. *Planetary and Space Science*, *58*(7), 1018–1025. https://doi.org/10.1016/j.pss.2010.03.007

Hadid, L. Z., Morooka, M. W., Wahlund, J.-E., Andrews, D. J., Shebanits, O., Kurth, W. S., et al. (2018). Saturn's ionosphere: Electron density altitude profiles and D ring electrodynamic interaction from the Cassini Grand Finale. *Geophysical Research Letters*, *45*. https://doi.org/10.1029/2018GL078004

Hamil, O., Cravens, T. E., Reedy, N. L., & Sakai, S. (2018). Fate of ice grains in Saturn's ionosphere. *Journal of Geophysical Research: Space Physics*, *123*, 1429–1440. https://doi.org/10.1002/2017JA024616

Havnes, O. (2002). Dusty plasmas in the ionosphere and its environment. In *Dusty plasmas in the new millennium: 3rd international conference on the physics of dusty plasmas* (Vol. 649, pp. 13–21). Durban, South Africa: American Inst. of Physics. https://doi.org/10.1063/1.1527732

Havnes, O., Antonsen, T., Hartquist, T. W., Fredriksen, Å., & Plane, J. M. C. (2015). The Tromsø programme of in situ and sample return studies of mesospheric nanoparticles. *Journal of Atmospheric and Solar-Terrestrial Physics*, *127*(C), 129–136. https://doi.org/10.1016/j.jastp.2014.09.010

Havnes, O., Surdal, L. H., & Philbrick, C. R. (2009). Mesospheric dust and its secondary effects as observed by the ESPRIT payload. *Annales Geophysicae*, *27*(3), 1119–1128. https://doi.org/10.5194/angeo-27-1119-2009

Hilgers, A., Holback, B., Holmgren, G., & Boström, R. (1992). Probe measurements of low plasma densities with applications to the auroral acceleration region and auroral kilometric radiation sources. *Journal of Geophysical Research*, *97*(A6), 8631–8641. https://doi.org/10.1029/91JA02193

Hoegy, W. R., Brace, L. H., Theis, R. F., & Mayr, H. G. (1980). Electron temperature and heat flow in the nightside Venus ionosphere. *Journal of Geophysical Research*, *85*(A13), 7811–7816. https://doi.org/10.1029/JA085iA13p07811

Holmberg, M., Wahlund, J.-E., & Morooka, M. W. (2012). Ion densities and velocities in the inner plasma torus of Saturn. *Planetary and Space*, *73*, 1.

Horanyi, M. (1996). Charged dust dynamics in the solar system. *Annual Review of Astronomy and Astrophysics*, *34*(1), 383–418. https://doi.org/10.1146/annurev.astro.34.1.383

Ivchenko, N., Facciolo, L., Lindqvist, P.-A., Kekkonen, P., & Holback, B. (2001). Disturbance of plasma environment in the vicinity of the Astrid-2 microsatellite. *Annales Geophysicae*, *19*(6), 655–666. https://doi.org/10.5194/angeo-19-655-2001

Jacobsen, K., Moen, J., & Pedersen, A. (2010). Quasistatic electric field structures and field-aligned currents in the polar cusp region. *EGU General Assembly*, *2010*(12), 13,127.

Kim, S.-H., & Merlino, R. L. (2006). Charging of dust grains in a plasma with negative ions. *Physics of Plasmas*, *13*(5), 052118–052117. https://doi.org/10.1063/1.2204830

Kliore, A. J., Nagy, A. F., Marouf, E. A., Anabtawi, A., Barbinis, E., Fleischman, D. U., & Kahan, D. S. (2009). Midlatitude and high-latitude electron density profiles in the ionosphere of Saturn obtained by Cassini radio occultation observations. *Journal of Geophysical Research*, *114*, A04315. https://doi.org/10.1029/2008JA013900

Kliore, A. J., Patel, I. R., Lindal, G. F., Sweetnam, D. N., Hotz, H. B., Waite, J. H., & McDonough, T. (1980). Structure of the ionosphere and atmosphere of Saturn from Pioneer 11 Saturn radio occultation. *Journal of Geophysical Research*, *85*(A11), 5857–5870. https://doi.org/10.1029/JA085iA11p05857

McDonald, J. N., & Williams, P. J. S. (1986). Electron temperature and electron density in the F-region of the ionosphere. I. Observed relationship. *Jounal of Geophysical Research*, *48*(6), 545–557. https://doi.org/10.1016/0021-9169(86)90088-7

McElroy, M. B. (1973). The ionospheres of the major planets (Article published in the Space Science Reviews special issue on "Outer Solar System Exploration - An Overview," ed. by J. E. Long and D. G. Rea.). *Space Science Reviews*, *14*(3), 460–473. https://doi.org/10.1007/BF00214756

Mitchell, D. G., Perry, M. E., Hamilton, D. C., Westlake, J. H., Kollmann, P., Smith, H. T., et al. (2018). Dust grains fall from Saturn's D-ring into its equatorial upper atmosphere. *Science*, *362*(6), aat2236. https://doi.org/10.1126/science.aat2236

Moore, L., Cravens, T. E., Müller-Wodarg, I., Perry, M. E., Waite, J. H. Jr., Perryman, R., et al. (2018). Models of Saturn's equatorial ionosphere based on in situ data from Cassini's Grand Finale. *Geophysical Research Letters*, *45*, 9398–9407. https://doi.org/10.1029/2018GL078162

Moore, L., Galand, M., Mueller-Wodarg, I., Yelle, R., & Mendillo, M. (2008). Plasma temperatures in Saturn's ionosphere. *Journal of Geophysical Research*, *113*, A10306. https://doi.org/10.1029/2008JA013373

Moore, L., O'Donoghue, J., Müller-Wodarg, I., Galand, M., & Mendillo, M. (2015). Saturn ring rain: Model estimates of water influx into Saturn's atmosphere. *Icarus*, *245*, 355–366. https://doi.org/10.1016/j.icarus.2014.08.041

Morooka, M. W., Wahlund, J.-E., Andrews, D., Persoon, A. M., Ye, S. Y., Kurth, W. S., et al. (2018). The Dusty plasma disk around the Janus/Epimetheus ring. *Journal of Geophysical Research: Space Physics*, *6*, 4668–4678. https://doi.org/10.1002/2017JA024917

Morooka, M. W., Wahlund, J.-E., Eriksson, A. I., Farrell, W. M., Gurnett, D. A., Kurth, W. S., et al. (2011). Dusty plasma in the vicinity of Enceladus. *Journal of Geophysical Research*, *116*, A04215. https://doi.org/10.1029/2011JA017038

Nagy, A. F., Chameides, W. L., Chen, R. H., & Atreya, S. K. (1976). Electron temperatures in the Jovian ionosphere. *Journal of Geophysical Research*, *81*(31), 5567–5569. https://doi.org/10.1029/JA081i031p05567

Nagy, A. F., Kliore, A. J., Marouf, E., French, R., Flasar, M., Rappaport, N. J., et al. (2006). First results from the ionospheric radio occultations of Saturn by the Cassini spacecraft. *Journal of Geophysical Research*, *111*, A06310. https://doi.org/10.1029/2005JA011519

O'Donoghue, J., Stallard, T. S., Melin, H., Jones, G. H., Cowley, S. W., Miller, S., et al. (2013). The domination of Saturn's low-latitude ionosphere by ring "rain.". *Nature*, *496*(7444), 193–195. https://doi.org/10.1038/nature12049

Persoon, A. M., Kurth, W. S., & Gurnett, D. A. (2018). Equatorial electron density measurements in Saturn's inner magnetosphere. *Geophysical Research Letters*, *32*. https://doi.org/10.1029/2005GL024294

Sakai, S., & Watanabe, S. (2016). Plasma dynamics in Saturn's middle-latitude ionosphere and implications for magnetosphere-ionosphere coupling. *Icarus*, *274*(C), 261–271. https://doi.org/10.1016/j.icarus.2016.03.009

Schunk, R., & Nagy, A. F. (2009). *Ionospheres*. Cambridge University Press. https://doi.org/10.1017/CBO9780511635342

Shebanits, O., Wahlund, J.-E., Mandt, K., Ågren, K., Edberg, N. J. T., & Waite, J. H. (2013). Negative ion densities in the ionosphere of Titan–Cassini RPWS/LP results. *Planetary and Space Science*, *84*, 153–162. https://doi.org/10.1016/j.pss.2013.05.021

Teolis, B. D., Niemann, H. B., Waite, J. H., Gell, D. A., Perryman, R. S., Kasprzak, W. T., et al. (2015). A revised sensitivity model for Cassini INMS: Results at Titan. *Space Science Reviews*, *190*(1–4), 47–84. https://doi.org/10.1007/s11214-014-0133-8

Tomsic, A., Marković, N., & Pettersson, J. B. C. (2000). Direct scattering and trapping-desorption of large water clusters from graphite. *Chemical Physics Letters*, *329*(3–4), 200–206. https://doi.org/10.1016/S0009-2614(00)01002-2

Vostrikov, A. A., Zadorozhny, A. M., Dubov, D. Y., Witt, G., Kazakova, I. V., Bragin, O. A., et al. (1997). Ionization of water clusters by collision with surface. *Zeitschrift Fur Physik D*, *40*(1-4), 542–545. https://doi.org/10.1007/s004600050273

Wahlund, J.-E., André, M., Eriksson, A. I. E., Lundberg, M., Morooka, M. W., Shafiq, M., et al. (2009). Detection of dusty plasma near the E-ring of Saturn. *Planetary and Space Science*, *57*(14-15), 1795–1806. https://doi.org/10.1016/j.pss.2009.03.011. https://doi.org/10.1016/j.pss.2009.03.011

Wahlund, J.-E., Morooka, M. W., Hadid, L. Z., Persoon, A. M., Farrell, W. M., Gurnett, D. A., et al. (2017). In situ measurements of Saturn's ionosphere show that it is dynamic and interacts with the rings. *Science*, *359*(6371), 66–68. https://doi.org/10.1126/science.aao4134

Waite, J. H. Jr., Perryman, R. S., Perry, M. E., Miller, K. E., Bell, J., Cravens, T. E., et al. (2018). Chemical interactions between Saturn's atmosphere and its rings. *Science*, *362*(6410), eaat2382. https://doi.org/10.1126/science.aat2382

Ye, S.-Y., Kurth, W. S., Hospodarsky, G. B., Persoon, A. M., Sulaiman, A. H., Gurnett, D. A., et al. (2018). Dust observation by the radio and plasma wave science instrument during Cassini's grand finale. *Geophysical Research Letters*, *45*, 10,101–10,109. https://doi.org/10.1029/2018GL078059